FAR ULTRAVIOLET IMAGING FROM THE IMAGE SPACECRAFT: 3. SPECTRAL IMAGING OF LYMAN-α AND OI 135.6 NM

S. B. MENDE, H. HEETDERKS, H. U. FREY, J. M. STOCK, M. LAMPTON, S.P. GELLER, R. ABIAD, O.H.W. SIEGMUND
Space Sciences Laboratory, University of California Berkeley, Berkeley, CA 94720
S. HABRAKEN, E. RENOTTE, C. JAMAR, P. ROCHUS
Centre Spatiale de Liege, Liege, Belgium B-4000
J.-C. GERARD
University of Liege, Liege, Belgium B-4000
R. SIGLER
Lockheed-Martin Palo Alto Research Laboratories, Palo Alto, CA 94304
H. LAUCHE
Max Planck Institut fur Aeronomie, D-37189 Katlenburg-Lindau, Germany

Abstract. Two FUV Spectral imaging instruments, the Spectrographic Imager (SI) and the Geocorona Photometer (GEO) provide IMAGE with simultaneous global maps of the hydrogen (121.8 nm) and oxygen 135.6 nm components of the terrestrial aurora and with observations of the three dimensional distribution of neutral hydrogen in the magnetosphere (121.6 nm). The SI is a novel instrument type, in which spectral separation and imaging functions are independent of each other. In this instrument, two-dimensional images are produced on two detectors, and the images are spectrally filtered by a spectrograph part of the instrument. One of the two detectors images the Doppler-shifted Lyman-α while rejecting the geocoronal "cold" Lyman-α, and another detector images the OI 135.6 nm emission. The spectrograph is an all-reflective Wadsworth configuration in which a grill arrangement is used to block most of the cold, un-Doppler-shifted geocoronal emission at 121.567 nm. The SI calibration established that the upper limit of transmission at cold geocoronal Lyman-α is less than 2%. The measured light collecting efficiency was 0.01 and 0.008 cm^2 at 121.8 and at 135.6 nm, respectively. This is consistent with the size of the input aperture, the optical transmission, and the photocathode efficiency. The expected sensitivity is 1.8 x 10^{-2} and 1.3 x 10^{-2} counts per Rayleigh per pixel for each 5s viewing exposure per satellite revolution (120s). The measured spatial resolution is better than the 128 x 128 pixel matrix over the 15° x 15° field of view in both wavelength channels. The SI detectors are photon counting devices using the cross delay line principle. In each detector a triple stack microchannel plate (MCP) amplifies the photo-electronic charge which is then deposited on a specially configured anode array. The position of the photon event is measured by digitizing the time delay between the pulses detected at each end of the anode structures. This scheme is intrinsically faster than systems that use charge division and it has a further advantage that it saturates more gradually at high count rates. The geocoronal Lyman-α is measured by a three-channel photometer system (GEO) which is a separate instrument. Each photometer has a built in MgF_2 lens to restrict the field of view to one degree and a ceramic electron multiplier with a KBr photocathode. One of the tubes is pointing radially outward perpendicular to the axis of satellite rotation. The optic of the other two subtend 60° with the rotation axis. These instruments take data continuously at 3 samples per second and rely on the combination of satellite rotation and orbital motion to scan the hydrogen cloud surrounding the earth. The detective efficiencies (effective quantum efficiency including windows) of the three tubes at Lyman-α are between 6 and 10%.

1. Introduction

Magnetospheric science aims to understand how charged particles, magnetic and electric fields interact with each other and how these interactions are modulated by external influences such as the solar wind and its magnetic field. The IMAGE spacecraft investigation will be the first program which will observe the magnetosphere only by remote sensing techniques. The IMAGE spacecraft carries several imagers, which use novel techniques that can image the plasma in the magnetosphere from a distant location. To assure that simultaneous auroral observations are made, several far ultraviolet imagers will also operate on the IMAGE spacecraft. In a companion paper we have discussed the general IMAGE FUV systems requirements and in another we presented the broad band FUV imaging with the FUV Wideband Imaging Camera (WIC) system. The main purpose of the FUV instrument set is to provide simultaneous global images of the aurora. In this paper we will discuss the FUV instruments which make

observations in specific wavelengths. at the Lyman-α emissions of atomic hydrogen and at the 135.6 nm emission of atomic oxygen. They are the Spectrographic Imager (SI) and the geocoronal (GEO) Lyman-α photometers.

2. Scientific Requirements

The Lyman-α emission line at 121.6 nm is produced by scattering of solar Lyman-α by the geocoronal hydrogen surrounding the Earth (Chamberlain, 1963). Measurement of its intensity with distance yields the geocoronal hydrogen distribution (Rairden *et al.*, 1986). The neutral hydrogen density component is needed for determining ion densities from neutral atom imagers. From neutral atom imager remote sensing measurements, the magnetospheric energetic ion distribution is inferred. The neutral fluxes measured by the neutral atom imagers are produced by charge exchange between the magnetospheric ions and the cold neutral background density. In order to invert the neutral atom imager data and obtain the original ion fluxes, the cold neutral background density must be measured. Measurement of the geocoronal emission is one way to obtain this background density. It was decided early on in implementing the IMAGE program that a separate Lyman-α photometer dedicated to geocorona measurements would be the best approach. The Geororona Photometer (GEO) will be discussed separately at the end of this paper.

Auroral Lyman-α emissions of neutral hydrogen are also produced by charge exchange of energetic protons which cascade into the atmosphere. (Eather 1967; Edgar *et al.*, 1973; Jasperse and Basu, 1982; Ishimoto *et al.*, 1989; Basu *et al.*, 1993; Strickland *et al.* 1993; Galand and Richmond, 1999). One objective of the IMAGE FUV instruments is the imaging of this type of Lyman-α emission.

As the protons penetrate into the atmosphere and collide with the atmospheric gas, they capture electrons from the major neutral constituents (N_2, O_2, O) through charge exchange reactions. They become fast neutral hydrogen atoms, some of which will radiate the Doppler-shifted Lyman-α emission. In subsequent collisions, the energetic H atoms may lose their electron in an electron stripping collision and reappear as protons, constrained in their motion by the magnetic field. The cycle will repeat hundreds to ten thousands of times depending on the primary proton energy.

Line profiles of the Lyman-α emission from proton precipitation have been calculated using a Monte-Carlo stochastic method (Marov *et al.*, 1997). The model solves the coupled Boltzmann differential equation for H^+ and H for arbitrary initial proton energy and pitch angle distributions. The collisions are calculated using all relevant differential cross sections and include consideration of angular deflection following collisions (non strictly forward scattering). The changes of pitch angle along the H^+/H path due to variations of the magnetic field, including proton mirroring, are taken into account. The effect of beam spreading due to the convergence of the field lines causing additional up-going particles is also included. The Lyman-α line profile is obtained by projecting and integrating the calculated velocity distribution function of the excited H atoms along the observation line of sight. The results of the calculations are illustrated in Figure 1.

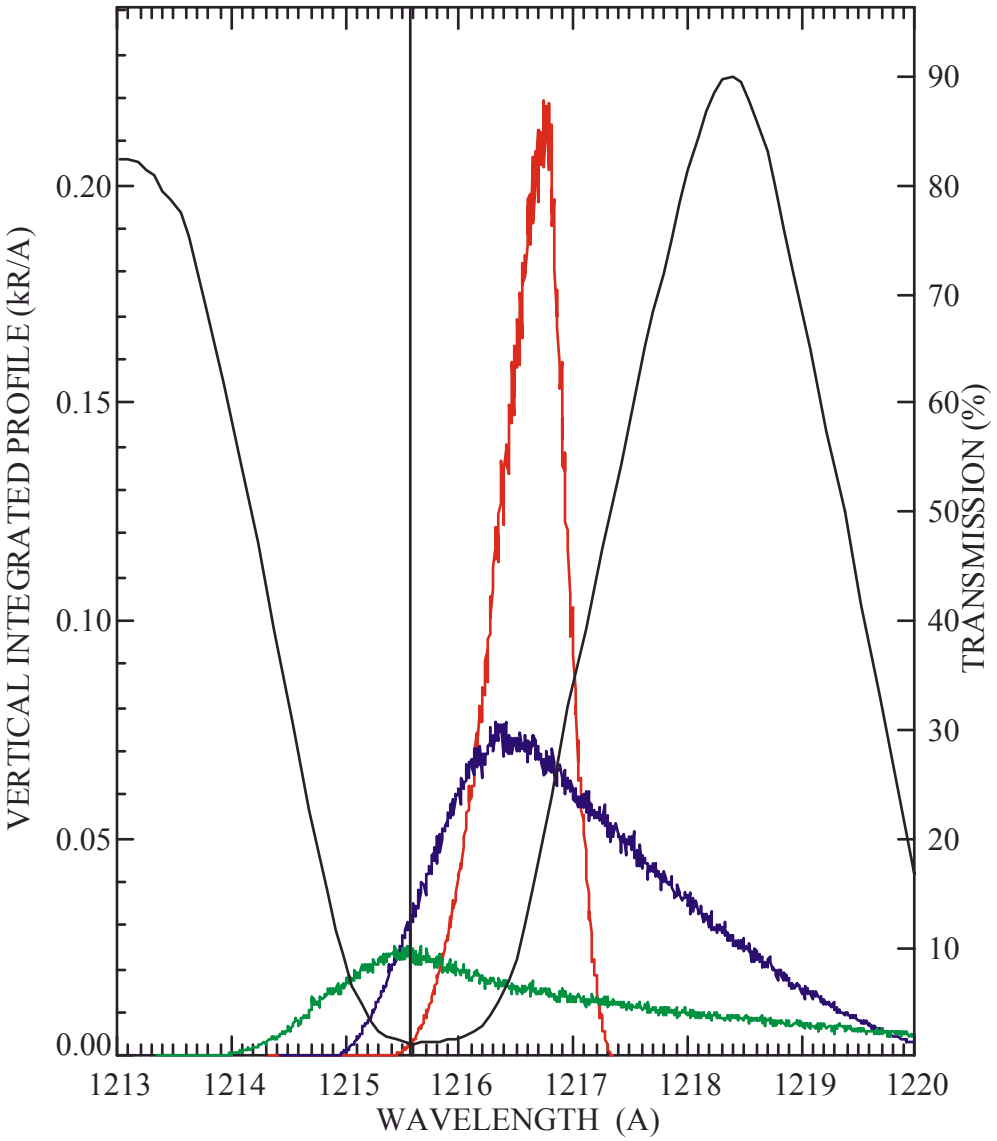

Figure 1. Calculated emissions profiles and the SI relative responsivity. The smooth curve represents the measured spectral transmission profile of the SI 1218 channel and the vertical line shows the rest Lyman-α wavelength. The tallest of the peaks represents the computed Lyman-α emission for protons of 1 keV mean energy, the middle one is 8 keV and the lowest one is 20 keV. They are normalized to the same energy flux.

From the calculations it seems clear that high spectral dispersion is a high priority because the greatest intensity emission is quite close to the cold Lyman-α wavelength. Unfortunately, the size and weight restrtictions of the spacecraft instrumentation limit the spectral resolution to about 0.2 nm, which means that efficient detection of protons will only occur at the higher, several keV energy range.

Precipitating electrons produce several other bright, discrete auroral emission features in the FUV range which favorably compete with the dayglow emissions (Strickland *et al.*,1983). Although the brightest line is the 130.4 OI emission, it is multiply scattered in the atmosphere and it is difficult to derive accurate two dimensional distribution of the auroral emissions. On the other hand, the 135.6 nm line is scattered only to a limited degree (Strickland and Anderson 1983) and is an excellent emission feature for imaging the aurora that can be related to the total electron precipitation. Thus, a primary measurement requirement for UV imaging is the detection and spectral separation of

the 135.6 nm emission from that of 130.4 nm. This requirement necessitated the use of a spectrometer because narrow band filter technology is not able to satisfy the requirement.

Requirements driving FUV SI design were:

(1) to image the entire auroral oval simultaneously with the magnetospheric images produced by the IMAGE spacecraft ,
(2) to separate spectrally the hot proton precipitation (Doppler-shifted Lyman-α emissions) from the intense, cold geocorona (Lyman-α emissions at 121.567 nm),
(3) to separate spectrally and image the 135.6 nm OI emission from the multiply scattered 130.4 nm emission.

These requirements necessitate efficient photon collection to produce a reasonable signal to noise ratio to permit the separation of the measured features from instrumental and natural backgrounds. However, the IMAGE FUV observations are made on a rotating platform, which stares at the Earth on a low duty cycle basis, and the relative faintness of the auroral emissions require the highest possible photon collection efficiency and instrument sensitivity. FUV imaging of the aurora from the rotating IMAGE spacecraft is possible because the spatial resolution requirement of the IMAGE mission is considerably less than on other missions (Anger *et al.*, 1987; Frank and Craven, 1988) such as the ISTP POLAR spacecraft, which had a dedicated Earth-staring platform (Torr *et al.*, 1995).

The first requirement forces a relatively large field of view: 15° x 15°. The second requirement necessitates maximizing the spectral resolution within the available resources, and an intrinsic spectral resolution of 0.2 nm was chosen to separate the Doppler-shifted auroral Lyman-α from the geocorona background. Since the Doppler-shifted Lyman-α signal is about 100 times less intense than the Lyman-α geocoronal emissions at 121.6 nm, internal scattering in the instrument must be minimized. To be able to interpret the Doppler-shifted auroral Lyman-α measurements in terms of pure proton aurora requires the rejection of nitrogen emissions near 120 nm (triplet lines at 119.955, 120.022, and 120.071 nm) ,which are produced by all auroras, including electron aurora. The third requirement provides that the transmission of the 130.4 triplet line should be less than 1% of the 135.6, necessitating an overall spectral resolution of better than 3 nm in the 130-135 spectral region.

The spatial resolution requirement specifies that, from 7 earth radii, the aurora oval shall be imaged with a resolution consistent with pixel size of 90 km x 90 km. This translates to an angular resolution of about 7 arcmin x 7 arcmin for each of the 128 pixels x 128 pixels, within the total field of view. In a general sense, optimization of the spectral behavior had higher priority than imaging qualities in the instrument design.

As discussed in the companion paper 1, an imager collects $10^6/4\pi$ = 80,000 photons per steradian per second per Rayleigh per cm^2 of input aperture. The 90 km pixel size at $7R_E$ defines the solid angle to be 4 x 10^{-6} sr, which is equivalent to Ω as referred to $A\Omega$ at the entrance aperture of the system. During a 5 s exposure the collection rate is 1.6 photons per pixel per Rayleigh per cm^2 of input aperture. Since proton auroras are of the order of less than 1 kR in Lyman-α it is important to maximize the sensitivity or equivalent aperture A_e of the instrument.

Table 1
IMAGE FUV SI and GEO Requirement Summary

	Wavelength (nm)	FOV (°)	Pixel size apogee (km)	Angular res. (°)	Photon collection efficiency times [exposure time] (Rayleigh^{-1} pix^{-1} cm^{-2})	Minimum Aperture for 1 count pix^{-1} for 100 R source strength (cm^2)
OI auroral morphology	135.6 with <1% 130.4 rejection	>10	100	0.13	1.65 [5 s]	0.006
Hydrogen aurora	121.8±.1 with 1215.667 rejection	>10	200	0.26	6.6 [5 s]	0.0015
Geocorona	121.6	360	N/A	1.0	5 [0.33 s]	0.002

3. The Spectrographic Imager (SI) Design

As originally proposed, the Spectrographic Imager would have used a classical configuration. However, during the initial design phases a novel approach emerged which offered a number of advantages over the classical system.

The classical configuration consists of a telescope, which images the Earth at its focal plane, followed by a spectrograph. The classical telescope has a slit in the focal plane that passes the central slice of the image into the spectrograph. The spectrograph collimates the light from the slit and a diffraction grating disperses the collimated light according to wavelength. The spectrometer camera optics focuses the light on the detector. Different wavelengths are diffracted in different angular directions and are spatially separated on the detector. The wavelength separation is in the direction perpendicular to the slit, while in the direction parallel to the slit the original luminosity distribution is preserved. Since the IMAGE FUV components are mounted on a rotating platform and the slit would be directed parallel to the axis of rotation, the slit would scan across the Earth as the satellite rotates.

There are a number of disadvantages with this classical approach.

1. The primary optics must have a large entrance aperture, A, to maximize the AΩ of the system and produce a bright image on the spectrometer slit. Note that Ω is independent of the physical properties of the instrument and was defined by the resolution requirement stated above. In the classical design the slit selects only a narrow region of potentially fully illuminated, generally circularly symmetrical optical field and most of the collected light is actually not used.
2. The spectral properties of the spectrometer and the imaging properties of the telescope have to be matched. The size of the slit determines both the field of view and the spectral resolution, and this condition constrains the choices of the system parameters. For example, using a wide slit for large spectral pass band may not support high spatial resolution and vice versa.
3. Bright emissions such as the geocoronal Lyman-α should be suppressed prior to reaching the detector because the detector's dynamic range would be seriously stressed and it might be difficult to see weak emissions in the spectral vicinity of Lyman-α.
4. The two instruments, the telescope optics and the spectrometer, would be physically in series, creating a long instrument less suitable for a small spacecraft.
5. Bright regions in the image would be in the slit field of view for a very short time, producing high instantaneous count rate which might saturate the system. Another system, which exposes the entire region simultaneously at an averaged count rate would be preferable, because most detectors are count rate limited.

A novel system, an Imaging Monochromator, was designed which removes most of these disadvantages. This system is illustrated in Figure 2.

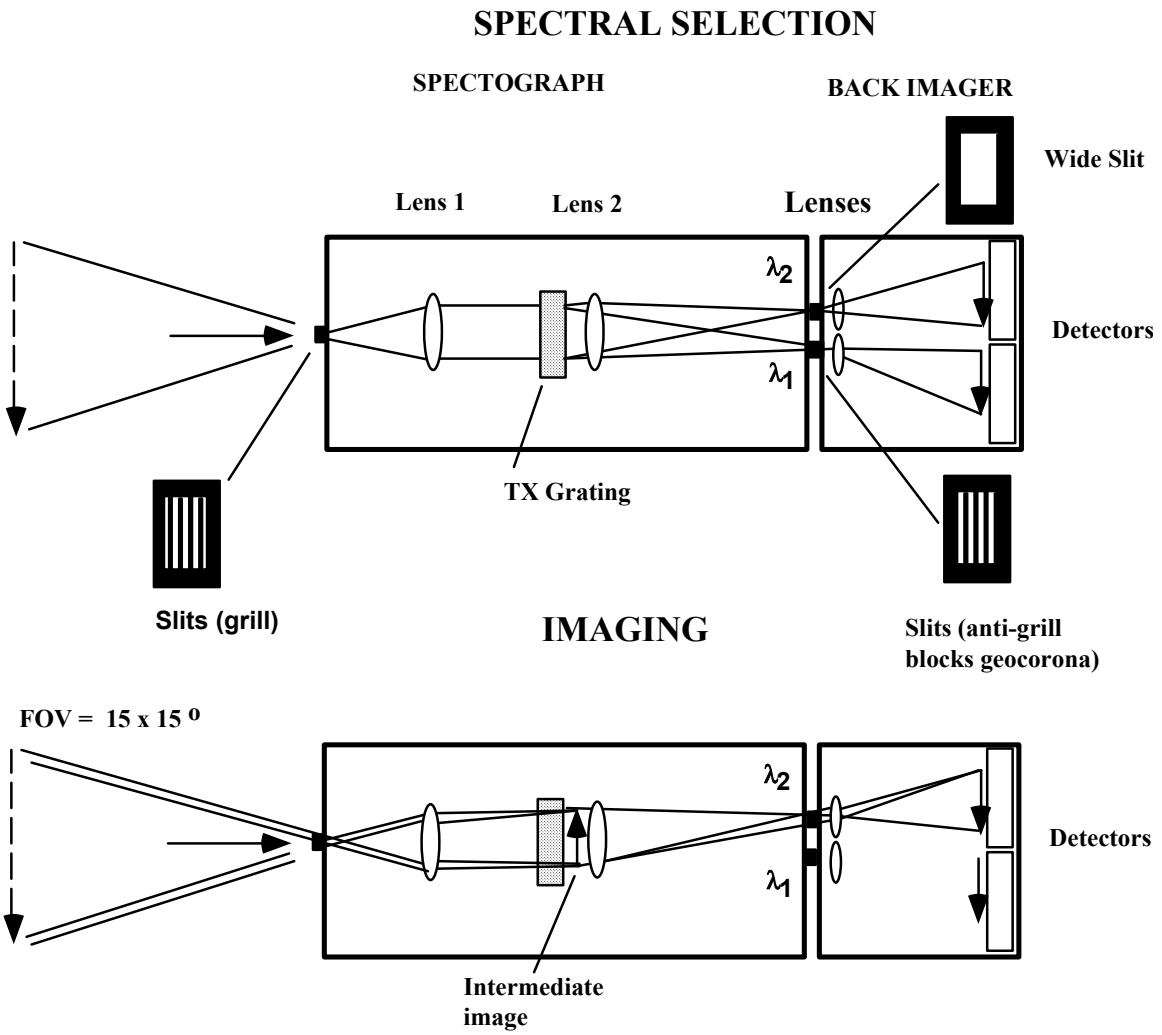

Figure 2. Illustration of the Imaging Monochromator concept. Top illustrates spectral filtering and bottom shows image forming. We have used refractive optical elements, lenses, to illustrate the principle of operation.

The top diagram in Figure 2 shows the wavelength selection and the bottom part shows imaging properties. This illustration of the imaging monochromator principle is intended to be fairly general and, for simplicity, we have used refractive lens elements to represent the optical components. In the IMAGE FUV instruments, all optical elements must be mirrors and, consequently, the optics is folded resulting in a more complicated arrangement. The first element in the imaging monochromator is an input aperture in the form of a slit (more specifically a grill of slits as explained later), followed by a collimating lens which produces parallel light from any point in the plane of the slit. The grating, in the case of this illustration, is a transmission grating placed at a distance from the collimating lens so that any parallel light coming through the slit is focused to a point at the grating. Thus, an image of the object at infinity in front of the instrument is formed close to the grating. The grating disperses the light according to wavelength. The wavelength-related angular dispersion of the light is the same for all points of the image. Thus, to a first order, imaging and wavelength selection are independent of each other. The grating is followed by a spectrograph camera lens, which focuses parallel light from the grating at the plane of the exit slit. A spectral region defined by the position and size of the slit(s) receives an equal amount of light from any point in the image. The last part of the system, the back imager, focuses the intermediate image, located at the grating, on the detector. The location and width of the exit slit(s) define the spectral region and the spectral width of the light passing through the system and therefore the spectrometer acts as an afocal filter in the optical system. In the IMAGE Spectrographic Imager, two wavelength regions were selected with two separate exit slits. One region is for imaging the proton aurora induced Doppler-shifted Lyman-α and the other is the 135.6 nm oxygen emission. The two regions in the illustration are denoted as $\lambda 1$ and $\lambda 2$.

The bottom of Figure 2 shows the imaging properties of the imaging monochromator. Parallel light entering the entrance slit (grill) from an object is focused at the plane of the grating. This intermediate image is re-imaged on the detectors by the back imager camera lens located behind the slit(s).

As we have discussed, the most remarkable property of this type of Imaging Monochromator concept is that its imaging and wavelength properties are independent of each other. This is because light rays leaving from a point of the intermediate image at the grating are brought in focus on the detector regardless of their direction or their associated wavelength. Different wavelengths are diffracted in different directions. The filtering is accomplished by the size and position of the slit(s). In this system it is possible, for example, to have a wide exit slit which passes a large spectral region combined with a sharp focus on the detector representing high spatial resolution. Thus, wide spectral passbands can be accommodated with high spatial imaging resolutions. Or vice versa, it is possible to use very fine spectral slits and integrate over large detector pixels.

It is also possible to have several separate wavelength channels using this approach. The arrangement needs separate back imager optics for each wavelength channel and each separate back imager optics has to provide some deflection to assure that the wavelength regions end up on separate detectors. For example, the two small re-imaging lenses in Figure 2 must be separate to assure that two pass-bands λ_1 and λ_2 form images at different locations and, if necessary, on separate detectors.

In order to have a fairly large throughput but high enough spectral resolution to discriminate geocoronal Lyman-α, the instrument needs a wide input slit which is subdivided into nine sub-slits forming a slit grill (Lemaitre *et al.*, 1984). The output slit of the Lyman-α channel also contains a similar slit grill which has been designed to block the light at the precise wavelength of the more intense cold geocoronal emission but "leak" profusely in the wavelength region near Lyman-α, passing the weaker Doppler-shifted emissions. Thus, the instrument has an efficient pass band for Doppler-shifted Lyman-α but strong rejection at geocoronal Lyman-α. The multiple parallel slits improve the light collection by a factor of nine and the IMAGE imaging monochromator is equivalent in efficiency to nine single slit instruments of the same size. This is a major advantage over the classical spectrograph type mentioned above.

The IMAGE Spectrographic Imager is schematically illustrated in Figure 3. The light enters the spectrometer through the entrance slit. The light is reflected by the collimator mirror, which produces parallel light from any point on the slit and focuses any parallel light coming through the slit at the intermediate image. This image is produced approximately at the grating. The function of the two imagers is to relay the intermediate image on two spatially separated detectors. Each back imager looks through its respective slits. The slit for the Lyman-α (121.8 nm) back imager is a pattern of slits which are designed to be in anti-coincidence with the input slit grill. The slit for the back imager labeled 135.6 is a plane wide slit.

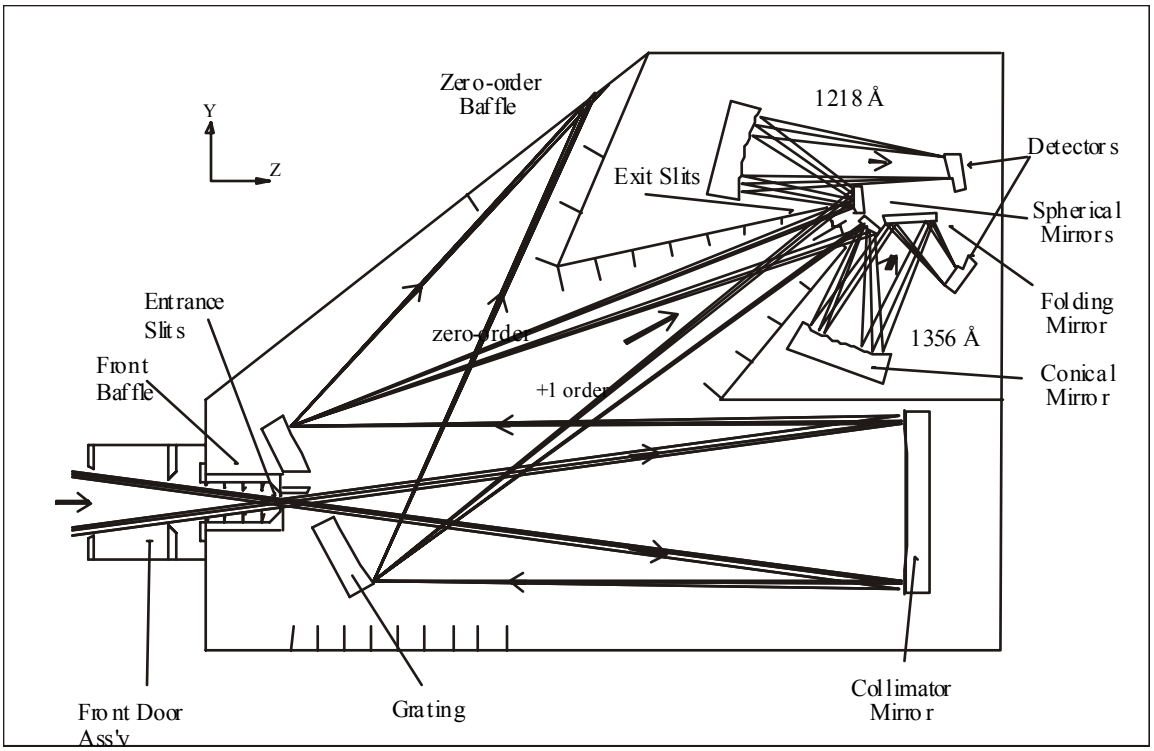

Figure 3. The IMAGE Specrographic Imager schematic.

The IMAGE Spectrographic Imager (Figure 4) had to be an all-reflective system to pass far ultra-violet radiation and to be achromatic over the wavelength range covered. To satisfy the spectral resolution requirements of 0.2 nm without lengthening the spectrometer, at least two surfaces were needed to provide sufficient aberration correction for the spectrograph. The instrument uses Wadsworth mounting in which a collimating mirror forms a parallel beam for a separate grating. The minimization of the aberrations also demanded the use of the central or paraxial, field of the collimator. This dictated using a system configuration in which the incoming light had to be on axis and had to pass through a central hole of the grating. The input slit grill, was placed very near the hole. Parallel light from the collimator reached the grating and it was diffracted into different directions according to wavelength. As we have discussed previously, this type of system forms an intermediate image at the grating. There are two exit slit sets. One is mounted in the region where the first order of Lyman-α appears and contains a grill for Lyman-α rejection. The other is located in the area where 135.6 nm emission appears and contains a wide-open slit for maximizing light throughput. The re-imaging optics is contained in the back imager. This module contains the various mirrors, which are needed to re-image the intermediate image produced on the grating.

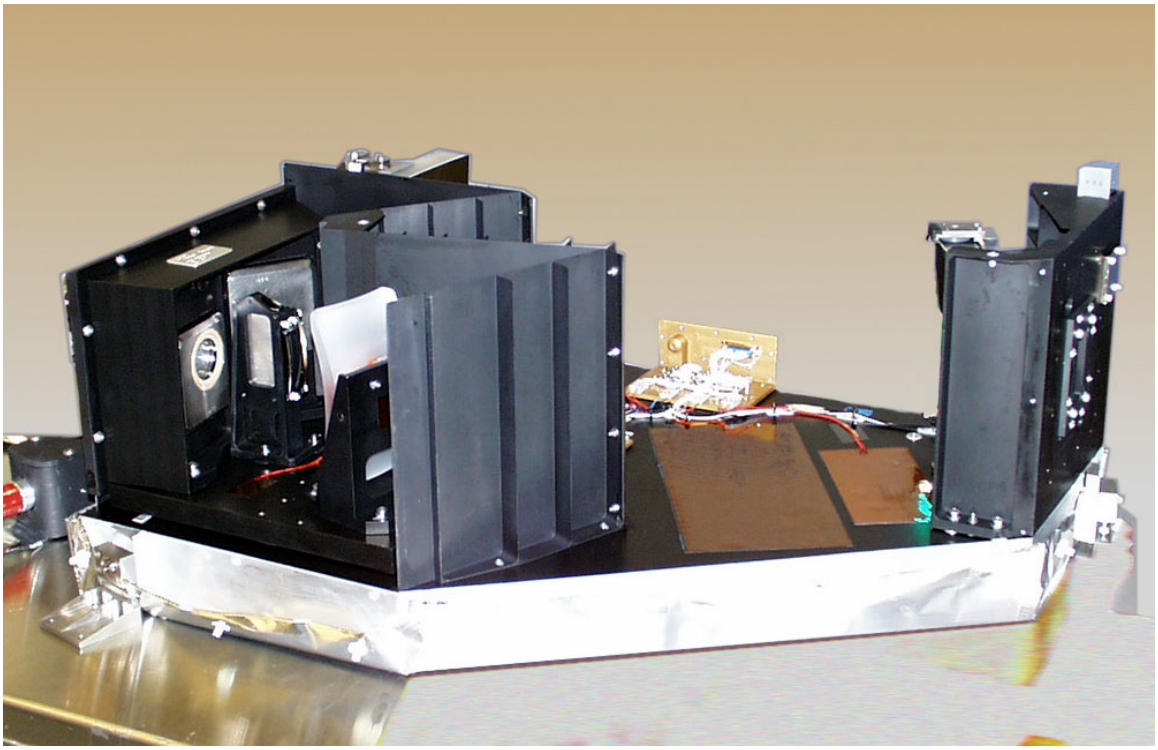

Figure 4. The Spectrographic Imager with its cover off.

The SI has a 3000 lines per mm holographically ruled grating of 181 x 156 mm in size (Table 2). Prior to building the flight gratings, the grating manufacturer, Zeiss, produced two smaller gratings. Both gratings were holographically ruled (3000 lines) but one of them was also subjected to ion etching process to produce a blaze. Both gratings were evaluated in the large vacuum chamber at UC Berkeley for grating efficiency and scatter. From these measurements it was evident that both gratings produced negligible diffuse scatter and that the ion etching process enhanced the grating effiency substantially. Thus, the flight grating was also ion etched.

In summary, the SI instrument takes spectrally filtered two-dimensional images. One of its two channels is filtered so as to suppress the geocoronal emission and enhance the Doppler-shifted proton aurora. On the spatial scale of the SI field of view and especially that of the proton aurora, the mean residual geocoronal background is uniform and its intensity can be estimated without any spectral separation.

The IMAGE Spectrographic Imager takes advantage of some of the properties of the imaging monochromator described above:

1. Maximum instrument performance with minimum size and weight: The collimating mirror acts as the primary optics and no separate large primary optics system is used. The long object distance of the back imager optics and the long focal length of the grating occupy the same space. Therefore, the same performance permits a much shorter instrument. To collect all the photons, the back imager optics had to be fast only in one dimension, the dimension parallel to the slit. Thus, the mirrors in the back imager could be reduced in size, quite narrow in the direction perpendicular to the slits.
2. Good spatial resolution with good light throughput using wide slits: The design allows high spatial resolution imaging with high throughput, wide slits. For example, in the observation of 135.6 nm emission, where a 3 nm spectral bandwidth is adequate in discriminating against 130.4 emissions, thus permitting a wide slit while maintaining high spatial resolution.
3. Exclusion of bright spectral features from anywhere near the detector: The design permits the removal of the bright geocoronal emission prior to entering detector space by using high precision slits and grills. This greatly reduces the background count rate.
4. Averaging the count rate during exposure: The system has a small input aperture but a wide instantaneous field of view. Thus, the detectors receive light simultaneously from a large spatial region. The system, therefore,

would function well with detectors that have counting rate limits even in the presence of small area bright regions.

The Spectrographic Imager system adopted for IMAGE has some disadvantages. For example, the instrument acts as a filtered imager and no information is retained about the spectral profile of the emission. It would have been valuable to obtain some wavelength distribution regarding the magnitude of the Doppler shift of the auroral Lyman-α emission. This necessitates the interpretation of the proton auroras in terms of an equivalent proton flux at the peak of the instrument sensitivity, which is 8 keV.

Another disadvantage is that the paraxial Wadsworth configuration needed a hole in the grating. This arrangement produced a blind region in the middle of the instantaneous image. In the IMAGE application, where a rotating platform is used and the instrument scans the image, the missing part of the image will be filled in during the rotation. The grating hole will produce a stripe of reduced intensity requiring normalization in the post flight data analysis. No other adverse effects are predicted due to the grating hole. During the development of the Spectrographic Imager we considered modifying the holographic ruling of the grating and correct the aberrations produced by an off-axis collimator. This would have allowed us to build the instrument without a hole in the middle of the grating. However, the computational results were discouraging, indicating that a considerably more complex system would be required and the attempt was abandoned.

For ease of manufacturing, two identical imagers were used: one working at 121.8 nm, the other one working at 135.6 nm. Each imager is a two mirror optical system. The first mirror is spherical. The second one is conical (elliptical) and works in an off-axis configuration. The two imagers are perfectly symmetric (only the back focal length is slightly different, due to geometry difference in the intermediate image to be relayed). So, two identical spherical, and two identical conical mirrors were manufactured. A flat folding mirror was added on the 135.6 nm imager so that the two detectors would fit in the available space.

The imagers are not optimized independently of the Wadsworth monochromator. Astigmatism, which was not critical for spectral selection at the exit slit plane, was the main aberration to be corrected by the imagers in order to generate the best possible image on the detectors.

This instrument is designed to minimize the 120 and 121.6 nm lines while transmitting the largest bandwidth in the region from approximately 121.7 to 122.3 nm. The grating angle and the collimator conic constant are optimized to reduce aberrations at 121 nm, i.e. between the 120 and 121.6 nm lines. It was relatively easy to meet the spectral resolving power requirements of the instrument in the 130-135 nm region to accomplish the 130.4 nm blocking for the second imager.

The linear dispersion is about 1820 μm/nm in the exit slit plane. For a 0.2 nm spectral resolution, the exit slit width is about 360 μm. The entrance slit width is (anamorphic magnification: 1/cos(grating angle)) about 400 μm. A compromise between throughput and aberrations level drove the entrance slit height to 36 mm. The Wadsworth monochromator is highly astigmatic. At the tangential focus the point spread function (PSF) is a thin line, parallel to the exit slit. Spectral performances are related to the width of that PSF line, not its length. For this reason, the astigmatism does not need to be corrected.

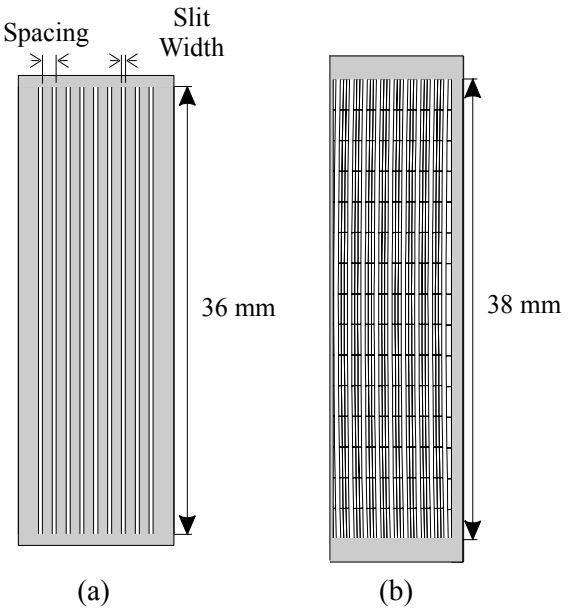

Figure 5 : Slits geometry. (a) : entrance slits (b) : exit slits

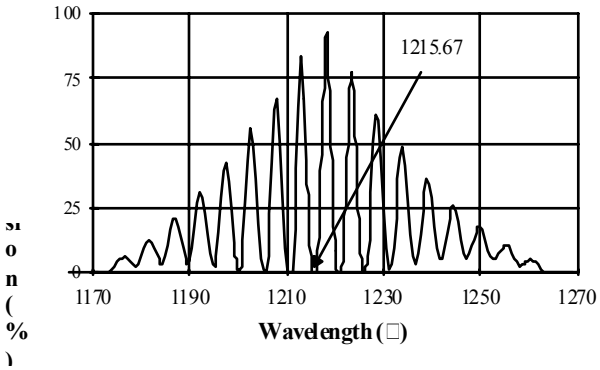

Figure 6 : Spectral filtering of the exit slit grill.

The slit configuration is specifically optimized to enhance the throughput (Figure 5). A grill with 9 slits is designed to stop the 120 and 121.6 nm (121.567 nm) lines, simultaneously (Figure 6). The slit spacing (period) is determined for this purpose: 0.5223 nm (i.e. one third of the wavelength difference between the two lines). The 120 and 121.6 nm images of the slits, at the exit slit plane, are perfectly superposed: the image of the first slit at 121.6 nm is superposed to the image of the fourth slit at 120 nm. This was important to block not only at 121.6 nm, but also electron induced emissions at 120 nm. Owing to the off-axis configuration of the Wadsworth, the exit slit image is slightly distorted (radius of curvature: ~1300 mm). Since the effect of such a curvature on a 36 mm slit is not negligible, a curved slit grill had to be manufactured. The slit width was optimized, compromising the throughput and the blocking efficiency. The present geometry specifies 0.19 nm wide slits, with masks (or bars) between slits 0.3323 nm wide. The focal plane and tilt of the exit slit assembly are optimized at Lyman-α. The actual dimensions of the entrance slits are related by the linear dispersion (182 μm/nm) and the anamorphic magnification defined by the grating angle (28°), giving a slit width of 391.6 μm and a spacing of 1076.6 μm or just over a mm. The exit slit grill does not require the anamorphic correction, but does require a tilt correction due to the tilt of the exit slit plane. The exit slit width is 356.5 μm. Table 2 lists the specifications of optical parts of the SI.

Table 2
Optical specifications of the SI elements

Mechanical Configuration

	Entrance slits	Exit slits
Overall slit width (μm)	391.6	356.5
Spacing (μm)	1076.6	980.1
Curvature	No	R = 1300 mm

Optical Equivalent

	Wavelength
Slit width	0.19 nm
Bar width	0.3323 nm
Slit spacing	0.5223 nm
Linear dispersion	1820 μm/nm.

Optical Design

	Radius of curvature (mm)	Conic Constant	Off-set (mm)	Size (mm) x	Size (mm) y
Collimator Mirror	1000 (concave)	-1.727	0	181	156
Grating	1000 (concave)	0	0	142	164
Spherical Mirrors	136.461 (convex)	0	0	52	20.25
Conical Mirrors	170.725 (concave)	0.114	53.5	144	76
Flat 135.6 nm	-	-	-	72	45.5

The SI optical configuration is quite unusual and it gives rise to irregular looking spot diagrams at the detector plane, with a non axi-symmetric Point Spread Function (PSF). The calculation of Encircled Half Energy Width (HEW) sometimes is not too meaningful. The HEW never exceeds 135 μm. The average value, over the whole FOV, is about 120 μm. The same results appear at 135.6 nm. We conclude that the imaging performances are within the specifications of the 140 x 140 μm^2 pixel size (128x128 pixel raster over the 18 x 18 mm^2 field), with a small margin for manufacturing and thermal tolerancing.

The spectral filtering of the monochromator is directly related to the slit imaging quality. As already mentioned, the image is highly astigmatic. The imaging quality is worse at 120 nm: RMS size about 200 μm at the slit center (x = 0) and 130 μm at the slit edges (x = ±18 mm). The spectral filtering will be significantly affected (see Figure 7).

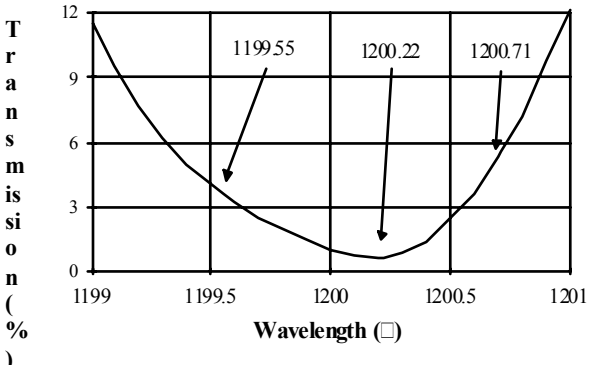

Figure 7: Spectral filtering performances in the 120 nm region.

Ray tracing was performed to evaluate the spectral filtering (or blocking) performances of the Wadsworth monochromator. The above calculations do not take into account the scattering level of the reflective surfaces (collimator and grating) as well as diffraction effects due to slit apertures.

The exit slit position was optimized, according to the fact that the 120 nm lines (119.955, 120.022, and 120.071 nm) are not as intense as the Lyman-α line (121.567 nm). It was specified that the 120 nm lines should never exceed 10% transmission. The calculated filtering quality is summarized in Table 3, and Figures 6-8:

Table 3
Calculated filtering quality of the monochromator with the optimized slit grill

Wavelength (nm)	Transmission (%)
119.955	3.6
120.022	0.65
120.071	5.5
121.567	0
121.82	93
122.09	0
122.35	77
122.6	0.1

The design considerations do not consider scattering and other deficiencies that occur in realistic systems. The following stray-light sources have been taken into account:

1. Direct light from outside the spectrometer towards the exit slits, at any wavelength.
2. Grating zero order diffraction at any wavelength.
3. Light from other diffraction orders, at a selection of critical wavelengths.
4. Light due mainly to scattering of the collimator and the grating.

The stray light reduction is performed by different methods (see Figure 3):

a. Black anodization of all parts. Although this is not too much help in the FUV it is effective in the visible and near UV region.
b. The back imager is isolated from the stand point of light tightness from the Wadsworth monochromator by special screens. Only the exit slits may transmit light from the monochromator to the imager zone.
c. A baffle is located in front of the entrance slits, attached to the front door assembly. The front door assembly itself is designed with vanes that reduce the unobstructed field of view.
d. Baffling with vanes to efficiently trap the zero order.
e. In the visible domain the grating does not produce any diffraction order (evanescence) except from the zero order.
f. If 250 nm < λ < 400 nm, the +1 order of the grating is illuminating vanes depicted at Figure 3 (at the bottom). Those vanes are designed to produce the required 10^{-6} reduction.
g. If 230 nm < λ < 250 nm, the +1 order is reflected back and, finally, passes through the grating hole (Littrow mounting).
h. If λ < 230 nm, several orders (-1, 0, +1, +2) with several directions (according to the wavelength) are present. Vane design is optimized for such a purpose.
i. Collimator and grating with low scattering level are desired (RMS roughness better than 1 nm).

Figure 3 shows a ray tracing at 121.8 and 135.6 nm including the zero and +1 diffraction orders only (for clarity). The depicted model of the FUV-SI was used to optimize the stray light reduction, with the ASAP software (trademark, Breault Research Organization, Inc.).

The SI resource requirements are summarized in Table 4.

Table 4
SI sensor head resource requirements

Mass	Dimensions	Standby power	Acquire

(kg)	L x W x H (mm)	(W)	Power (W)
20.9	800 x 515 x 300	0.96	2.16

4. SI instrument performance

The Wadsworth spectrograph was calibrated prior to installation of the back imager. Monochromatic light from a Lyman-α lamp produced a diffuse beam at the entrance grill of the instrument and a photomultiplier was placed behind the Lyman-α output slit-grill to measure the transmission of the monochromator. The entrance slit was moved in a direction perpendicular to the slits. This provided an effective wavelength scan of the instrument transmission. Figure 9 shows the theoretical transmission spectrum based on ray tracing compared with the measured transmission. Note that the wavelength scale is obtained by translating linear motion of the grill into wavelength using the dispersion of the instrument as 1820 μm/nm at the exit plane which translates to 2061.3 μm/nm at the entrance slit plane.

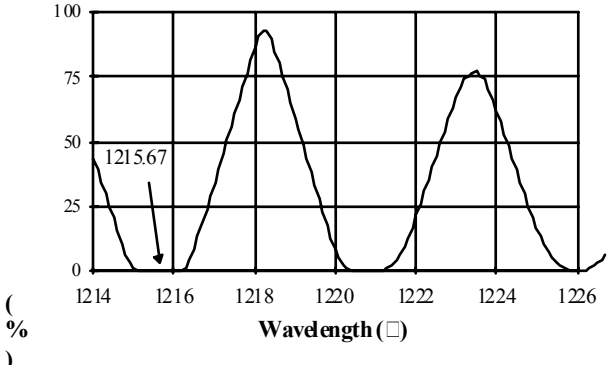

Figure 8: Spectral filtering performances in the 121.6 nm region.

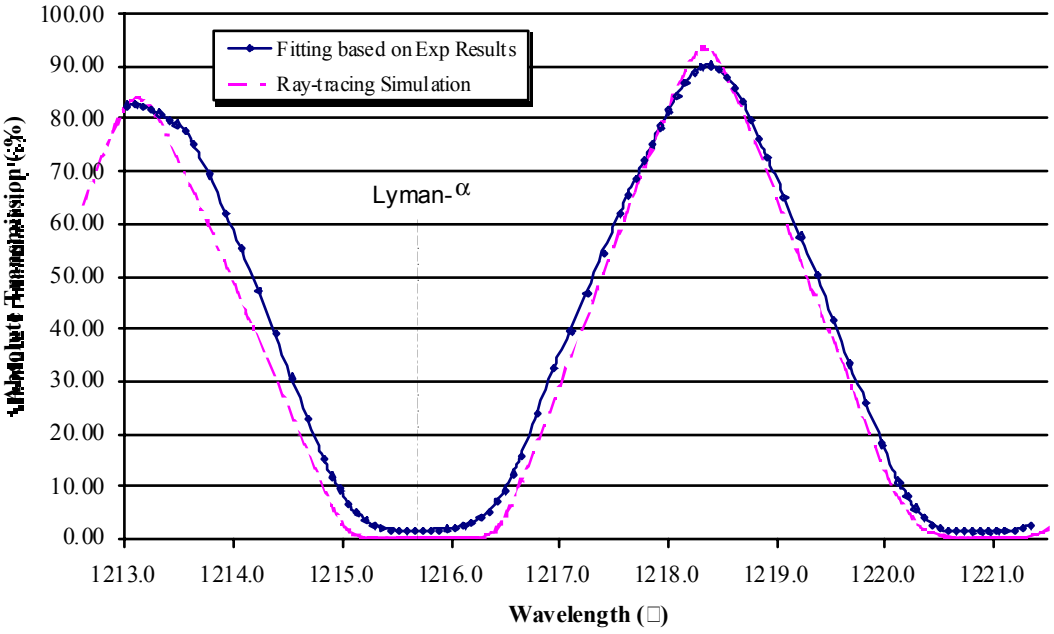

Figure 9. The transmission of the Wadsworth spectrometer at Lyman alpha when measured with a photo-multiplier at the exit grill. Unfortunately, the sources was not truly monochromatic Lyman alpha.

The minimum of transmission, i.e. the Lyman-α leak, is 2.3%. That is higher than expected. Since the full width at 10% maximum has not significantly increased compared to measurements with test slits, we do not suspect a high level of unwanted light that would come from a slit grill matching error, or from optical aberrations. Actually, the lamp spectrum is not as monochromatic as expected. With the help of a vacuum monochromator (1-meter Rowland type), a significant radiation level was measured out of the Lyman-α thin emission line. Since the SI12 channel has a transmission spectrum that extends from 117.5 to 126.5 nm (Figure 6), any radiation inside that bandwidth is affecting the background count. When the lamp spectrum is taken into account, we calculated that this instrument is able to efficiently filter a pure Lyman-α emission with a residual transmission of 1.3%, instead of 2.3%. It should be noted that the calibration lamps also produce residual H_2 emissions that are very close in wavelength to Lyman-α. Unfortunately, we did not possess a vacuum monochromator that had a higher wavelength resolution than that of the SI flight instrument, and it was not possible to measure the true instrument rejection. The measurement of 1.3% is a worst case scenario.

During a special tune up procedure, the instrument was placed in the vacuum chamber and tuned for best rejection by remote actuator adjustments for moving the slit. When the best Lyman-α rejection was reached the movement was blocked and the adjusters removed. As part of the environmental qualifications of the SI instrument the Lyman-α rejection was re-verified at operational temperature extremes and during post vibration functional tests.

The imaging performance of the SI was also calibrated. A UV monochromator was illuminated by a broad band UV source. The exit slit (pinhole) of the test monochromator was picked up by an off-axis paraboloid collimator mirror and parallel light was directed into the entrance aperture of the SI. The whole system including the SI instrument was in a vacuum chamber. With this test setup, we could study the imaging performance of the SI as a function of wavelength.

Figures 10 and 11 show the FWHM for the FOV mapping at 121.8 and 135.6 nm, respectively. Results depict that the FWHM is about 100 μm at 121.8 nm and 110 μm at 135.6 nm. It means that the angular resolution of the SI is 5 arcmin (15° over 128 pixels = 7 arcmin.) on both wavelength bandwidths. These measurements were also performed at the operational temperature extremes during thermal vacuum test.

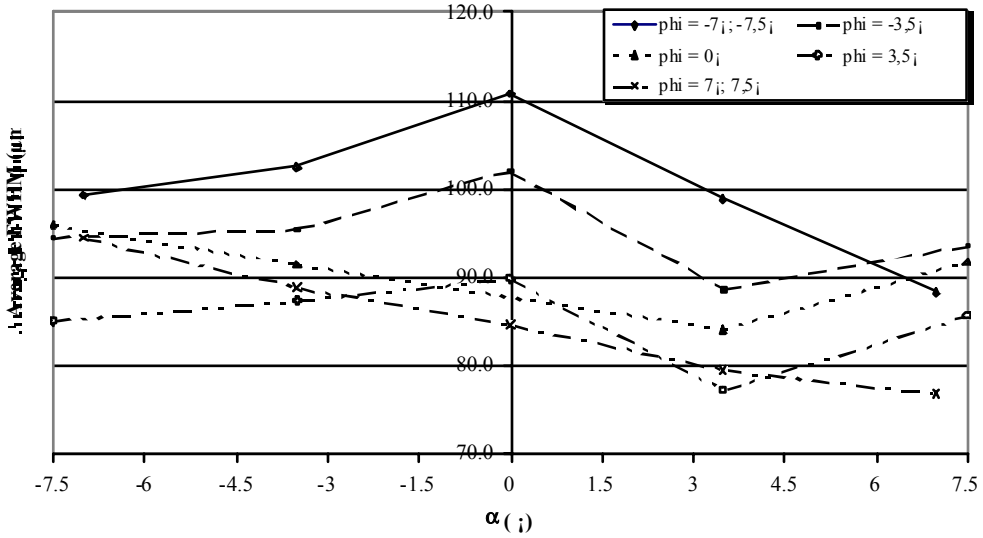

Figure 10: Plot of the FWHM at 121.8 nm for several FoV inside the useful range. ϕ and α denote the angles representing directions approximately parallel and perpendicular to the spacecraft spin axis.

The intrinsic spatial resolution of detectors was determined by stimulated image spots (using a pulse generator). The FWHM is about 20 μm, on both axis and both detectors, which is equivalent to about 1 arcmin angular resolution.

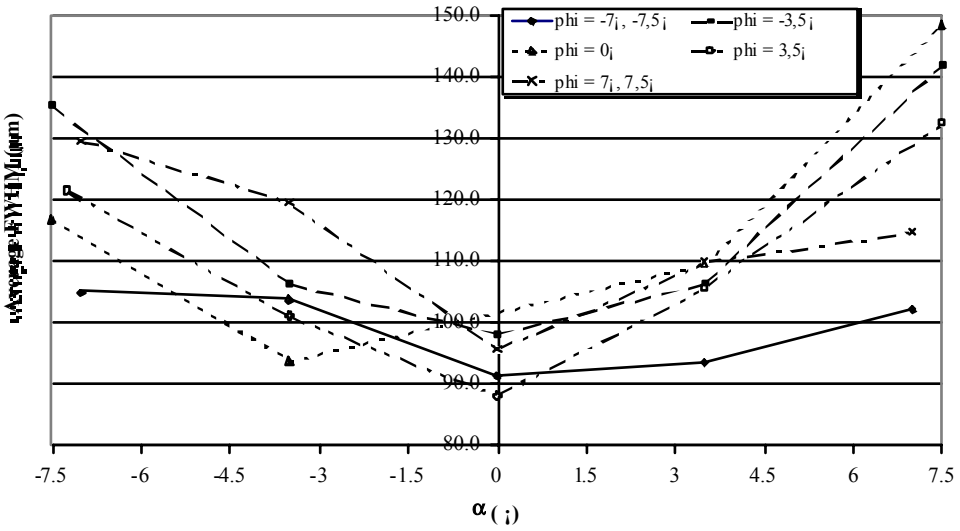

Figure 11: Plot of the FWHM at 135.6 nm for several FoV inside the useful range.

The SI performances shown in Figures 10 and 11 are a combination of intrinsic detector resolution, collimated beam divergence (1 arcmin angular resolution), and optical resolution of the SI. These figures prove that the optical parts of the SI were successfully polished, assembled and aligned. There is no significant difference between the experimental results and the theoretical values. In these figures, we define average FWHM as $(FWHM_x \times FWHM_y)^{1/2}$.

4.1. Absolute Response Calibrations of the SI

An argon-filled lamp was used as a spectrally diffuse source and the radiation passed through a vacuum monochromator of 0.2 nm spectral resolution. The exit slit of the monochromator was coupled to a collimator, also inside the chamber, which then produced a beam entering the SI. The beam could be intercepted by an absolutely calibrated photo multiplier tube (PM) that was on a rotation stage and could be moved in and out of the beam. The principle of the measurement was that the PM tube measured the input flux of photons, which was compared to the SI detector image total flux. The results of the measurements for the Lyman-α wavelength region are illustrated in Figure 12 and for 135 nm in Figure 13. The polarization dependence introduced by our calibration preselector grating has been ignored because the polarization effects are small near normal incidence (Loewen and Popov, 1997).

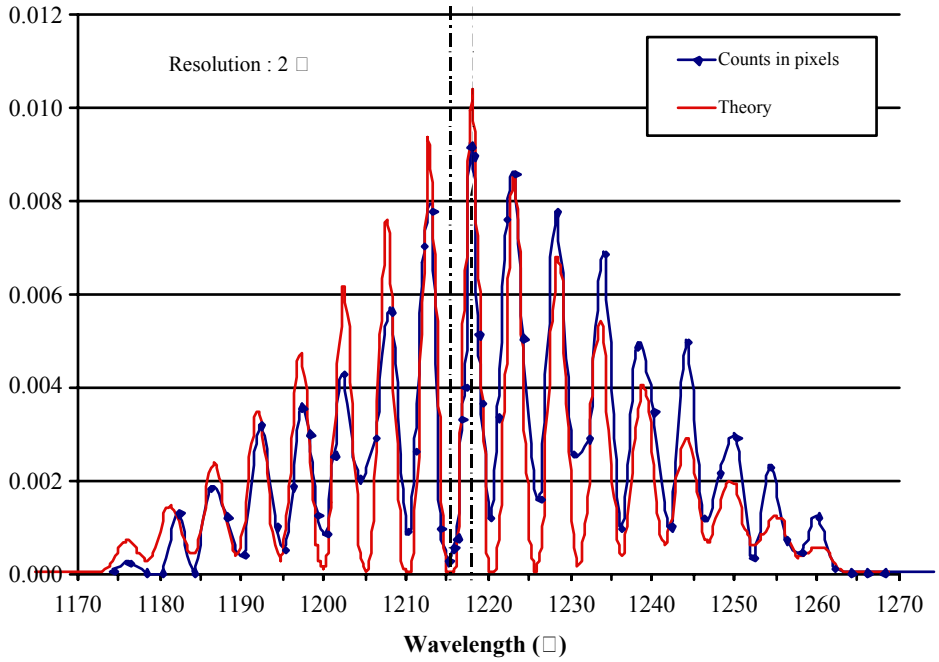

Figure 12. Transmission as a function of wavelengths for the 121.8 nm channel. The source monochroomator spectral resolution is .2 nm.

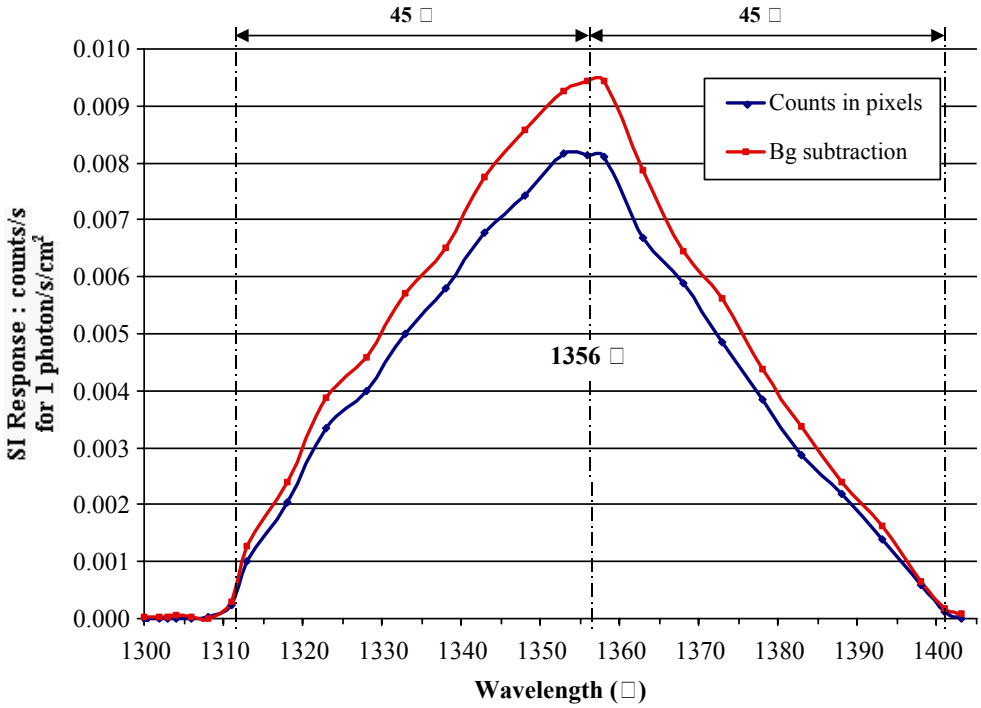

Figure 13. Absolute response of the SI near 135.6nm.

From the data we can see that the measured responses are about 1.1% at 121.8 nm and about 1% at 135.6 nm. This is consistent with a detector photocathode efficiency of 17% at 121.8 nm and 14% at 135.6 nm. The entrance aperture slit grill is about 1 cm^2 open area. Therefore, taking the earlier derived 1.6 photons per Rayleigh shows that the overall efficiency of the instrument is about 1.6 x 10^{-2} counts per Rayleigh per pixel for a 5 s exposure in the 135.6 nm channel and 1.8 x 10^{-2} in the Lyman-α channel.

The instrument routinely transmits sample pulse height distributions in the housekeeping data. During the on orbit operation of the instrument this will be monitored routinely and the high voltage of the MCPs adjusted to assure that the SI instrument detection threshold will be kept closely to the same level as it was during pre-flight calibration. It should be noted also that the nature of orbit and the spacecraft rotation will assure that the same FUV stars will be observed spin after spin during the entire mission. These stars will provide an excellent intensity reference throughout the operation of the SI instrument.

4.2. The detector system for the Spectrographic Imager

A set of compact microchannel plate detectors was developed utilizing a cross delay-line readout system for the IMAGE FUV Spectrographic Imager. Two detectors are required for the two pass bands. Both detectors are nearly identical, the only difference being the position of the input window on the detector cover plate. Each detector, optimized for operation in the far ultraviolet with a KBr photocathode, provides high spatial resolution and good linearity over a 20 mm square format.

The SI crossed delay line (XDL) detectors (Lampton *et al.*, 1987) have a long heritage at U.C. Berkeley. For example, a similar XDL detector was built for the SOHO mission, which has operated successfully for 2+ years. (Siegmund *et al.*, 1994).

The requirements for the SI detectors are shown in Table 5.

Table 5
SI Detector Properties

Attribute:	Requirement:
Active area (photosensitive area)	20 mm x 20 mm
Sensitivity (QE)	20%-121.6 nm, 10%-135.6 nm (w/o window)
Response uniformity	±20%
Digital pixels at the time delay converter	1024 x 1024 super samples for TDI scanning
Linearity	±50 μm
Detector resolution	60 μm
Maximum count rate (system)	10^5counts/s
Maximum single pore rate	1 count/s
Background rate	2 counts/s/cm^2

The principle of the XDL detector is illustrated in Figure 14. An XDL image sensor comprises a microchannel plate (MCP), a two-dimensional delay line anode, four pulse amplifiers, four timing discriminators, and two time interval measuring circuits. In the figure we show only the vertical anode set with its corresponding amplifiers at each end of the anode array. In operation, an electron avalanche from the MCP deposits a charge cloud on the anode. The charge divides into equal portions travelling opposite directions within the anode. The output pulses have a timing delay (t_1 and t_2) that is linearly determined by the event centroid position. Each anode output feeds a pulse amplifier whose bandwidth (a few hundred MHz) controls the system noise performance and pulse shape. A fixed delay is built into one leg of the X pair and one leg of the Y pair to create a start-stop asymmetry to assure that the stop always follows the start. A timing discriminator is connected to each of these start and stop signals. The logic output of these discriminators drives time interval digitizers that recover each event's coordinates in real time. The accuracy of the position location by this type of detectors and the circuits is ~40 μm (Lampton, 1998; Stock *et al.*, 1998).

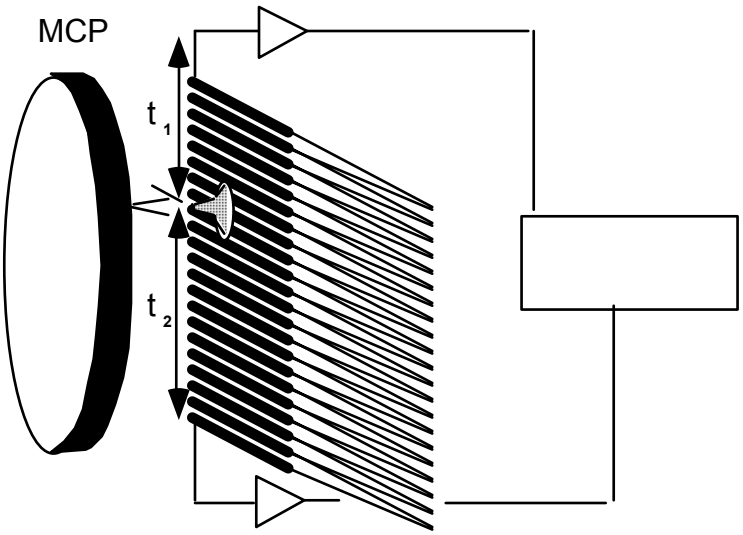

Figure 14. The principle of the XDL detector.

The XDL readout system was chosen to allow high counting rates and provide good resolution and linearity. These requirements would be difficult to achieve using other schemes encoding the position. The front-end electronics (amplifier and high voltage power supply) are bolted directly to the detector head and are packaged in a compact design favorable for the tight space constraints imposed by the SI instrument. For simplicity and cost reasons the microchannel plates are circular 36 mm plates, with an input 20 mm square mask. Quantum efficiency for the far ultraviolet is enhanced by a KBr photocathode applied directly to the surface of the MCP.

The MCP stack is a Z configuration of 3 MCPs with a pore length to width ratio of 80:1. The plates are Photonis-SAS 36 mm diameter, low resistance plates (~30 MΩ) with 12.5 μm pores, 15 μm center to center pore spacing, and 13° pore bias. Low resistance plates were chosen to provide fast recovery times for electrons in the MCP during periods of high local and global counting rates. The MCPs were baked and scrubbed prior to application of the photocathode, common practices for conditioning microchannel plates. It was elected not to subject the MCPs to a rigorous scrub as the detector will be accumulating data in orbit in a scanning manner, distributing would-be localized gain losses evenly over one dimension of the scanning direction of the active area. The photocathode, 1μm thickness of KBr, was deposited directly to the surface of the microchannel plate, coating the walls of the pores a few pore diameters deep. The techniques used to apply the photocathode and measure its efficiency are established as part of our photocathode development program (Jelinsky *et al.*, 1996) and were used for previous flight programs.

The detector system is illustrated in Figure 15. The cover plate with the MgF_2 window was removed and the inside was exposed. The circular region in the top right hand corner is the MCP stack with a square mask covering it. The black square area in the middle is the sensitive part of the MCP. The rectangular areas below and to the left of the MCP stack are the serpentines of the delay lines, one for the X and the other for the Y detection. The high voltage feed-through is visible at the bottom left. The black hole at bottom right is the pumping port for the detector.

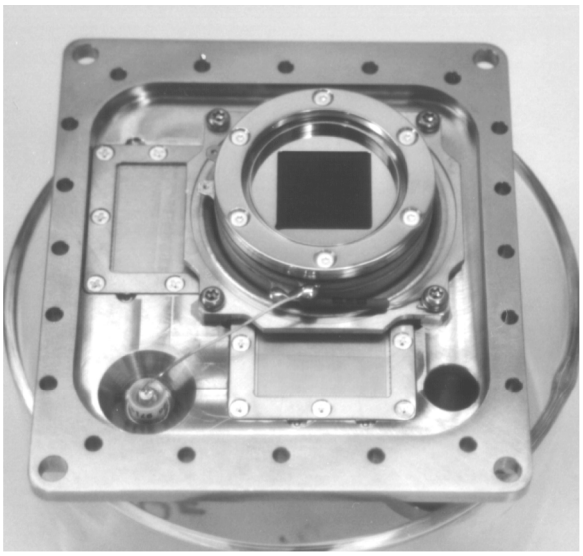

Figure 15. SI XDL detector without cover. Dark square is MCP active area.

The XDL anodes used for the SI detectors (shown in Figure 16) were fabricated using a new technique, in which the two delay lines charge collection fingers (for one axis) were plated onto a 0.38 mm thick alumina substrate. Subsequent layers of insulators and conductors that define the other set of charge collection fingers (and other axis) were then applied, one by one, crossing the existing fingers. The last layer is the upper set of copper fingers, attached to its lower delay line. The fingers are approximately 0.3 mm in width (wider for the lower fingers) with a 0.6 mm period. Each delay line has a width of 0.2 mm and a gap of 0.1 mm between the traces of the serpentine. The fabrication process was finalized by plating on a protective layer of gold.

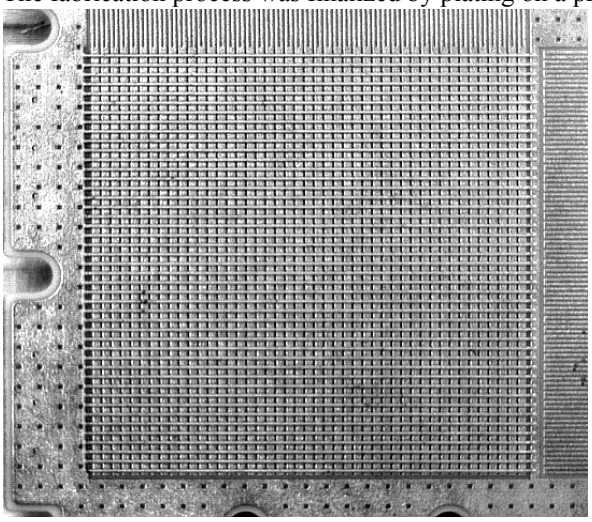

Figure 16. XDL anode. Only the active square is shown. The serpentine delay lines at the top and on the right are cut off in the figure presented here.

4.3. Microchannel plate gain characteristics

Desirable MCP characteristics for position encoding systems include reasonably high gain (10^7 e-) and narrow pulse height distributions. However, unlike charge division position encoding, for example, the timing electronics for delay line readouts are more tolerant to lower gain for high resolution performance, relaxing the requirement for SI to push to the highest gains (and voltages) possible. Figure 17 shows typical gain and pulse height characteristics for the SI detector MCPs. The detector was illuminated with a 253.7 nm mercury lamp. Efforts were made to minimize gaps between the MCPs during stacking, resulting in very favorable pulse

height distributions for both flight detectors, distributions that were repeatable after disassembly and re-stacking. We find these MCPs provide ample gain and an operating margin compliant with the pulse height requirements of TDC. The MCPs were also operated at high local and global counting rates to ensure that there was no evidence of gain "depression". This effect has been documented in other studies (Siegmund and Stock, 1991) and shows that for low resistance MCPs such as these the onset of gain depression will occur at count rates much higher than those expected for the SI.

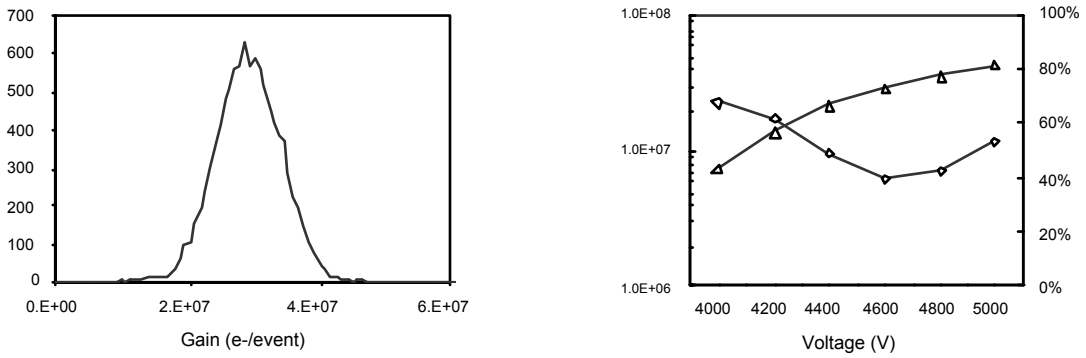

Figure 17. (left) Typical MCP gain spectrum. (right) Typical MCP gain voltage characteristics. The line marked by triangles shows the gain and the line with crosses shows the FWHM.

Owing to the modest mission-average count rates and the fact that the auroral oval is dynamically scanned across the detector, the local charge extraction by photoevents is not severe. For example, an average 1kR flux over 1% of the pixels will use about 0.01 coulomb/cm^2. Judging from previous long-duration missions, it is expected to see little or no reduction in detector gain during the mission. Nonetheless, the detector pulse height distributions are continually monitored and both the detector HV bias and the signal discriminator settings can be altered by remote telecommand if necessary.

4.4. Resolution and linearity performance

Figure 18 shows pinhole images of the XDL detectors taken with a pinhole mask placed directly on the MCP stack. The pinhole diameters are 10 μm with a position accuracy of ±15 μm. As can be seen in the accompanying histogram, the detector resolution is approximately 40 μm FWHM; this holds true for about 90% of the image. Near the edge of the image (outside 1 mm) the resolution worsens to 35 μm. The Y resolution is generally better than X (about 20%) with some pinholes measuring as small as 15 μm. This is most likely due to the fact that the Y pulses are larger, producing higher resolution due to better signal to noise or better matching of the signal to the timing electronics, or both. The Y pulses are larger because more charge is collected by the wider Y stripline. This result is inconsequential for SI but may be a desirable trait for other XDL detectors where resolution requirements may be different for each axis. In this case it may be advantageous to use a narrow upper stripline, for example, to allow more charge to reach the lower.

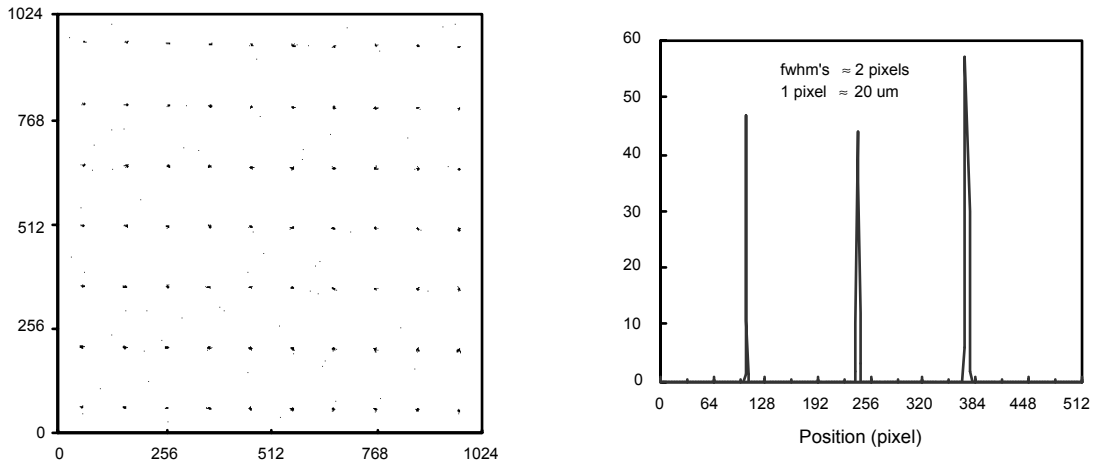

Figure 18. Pinhole mask image using IMAGE SI TDC (left). Typical histogram of 3 pinholes (right).

In the case of the IMAGE TDC, the digitization is coarser, approximately 20 μm /pixel, so most of the data is only in a few pixels. Without adjustments in the TDC for walk, the pinhole widths are determined to be 2-3 pixels (40-60 μm) wide, acceptable for our requirements. The TDC tested does not have its Y scale matched to the particular detector used, and so the entire detector is not imaged. Final scales had to be set when the detectors were integrated with the flight electronics.

From the pinhole images it is determined that the linearity of the imaging is better than ±50 μm over 90% of the image. This worsens to 100-200 μm at the outside 1 mm edge of the anode, particularly near the corners. This is due to the fact that charge from the bottom of the MCP stack is close to the circular flange supporting the MCP stack, producing an edge field effect commonly seen in microchannel plate devices. This is not perceived to be a problem as the SI FOV is 18 x 18 mm^2 therefore generally inside the 1 mm of the edge of the detector active area. Also, distortions are to be included into a distortion matrix that is applied to each pixel location in the flight software.

4.5. Flat field response

Figure 19 shows a flat field image of one XDL detector taken at 512 x 512 pixel resolution with commercial timing electronics. Noticeably absent from the image is the pattern of hexagonal multifiber boundaries characteristic of many MCP flat field images. This is not uncommon for smaller MCPs like these as they undergo a manufacturing process that is less likely to produce noticeable line defects at the multi-fiber boundaries. The MCPs were stacked so that the planar orientation of the pore bias of the top MCP was only rotated 150° from the middle plate instead of 180° such as between the middle and bottom plate. As suggested in testing during our previous flight programs, and more recently in a detailed study, this nearly eliminated all of the Moire effects commonly seen in stacked MCP sets. Evidence of very small-scale Moire is evident in the full resolution image but is not discernable in the figure printed here. Quantified in the accompanying histogram (taken from the full resolution image), periodic modulation is not evident and the few percent of noise is statistics. Background rates for both detectors are < 5 cps in the photosensitive area (< 1 cps/cm2). The corner bulge is due to a small scallop machined into the aperture mask that provides a fixed mechanical reference on the image. Illumination was with a 253.7 nm UV lamp. We conclude by stating that the SI instrument calibration data demonstrated that the XDL detectors are performing to specification.

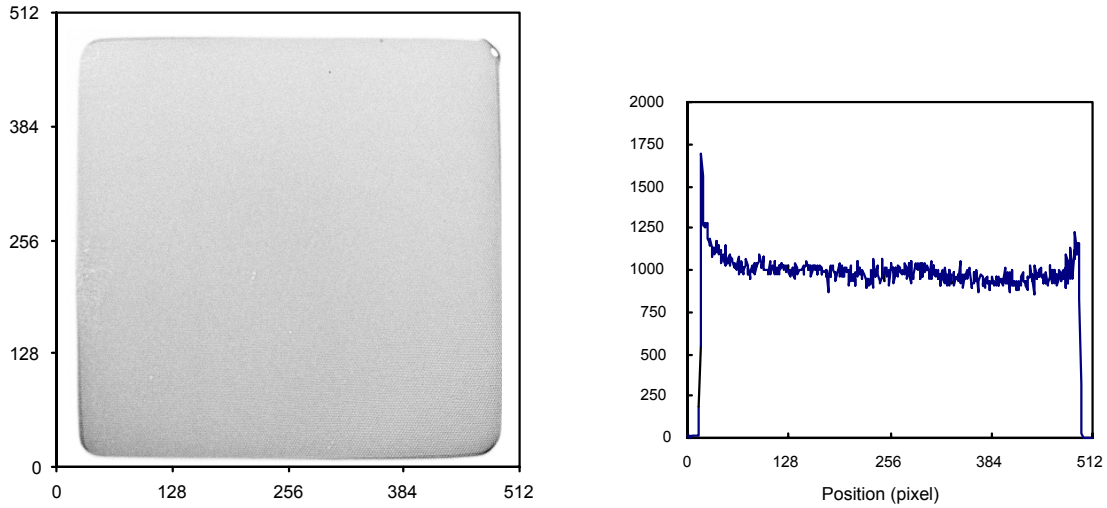

Figure 19. Flat field of XDL detector (1356). 20 Mcnts (left). 10 pixel histogram of flat field (right).

5. The GEO instrument

The main constituent of the exospheric space around Earth is neutral hydrogen. Resonance scattering of solar light produces bright hydrogen Lyman-α radiation, called geocorona. This has been investigated from several spacecraft using mostly photometers (see e.g. Meier, 1991; Rairden *et al.*, 1986). Owing to the large-scale height of hydrogen, significant concentrations can still be found at geocentric distances of several Earth radii.

One of the main goals of the IMAGE mission is the detection and imaging of energetic neutral atoms generated by charge-exchange interaction between the ring current and the geocorona. A quantitative investigation of this charge exchange reaction requires the exact knowledge of the neutral hydrogen atom concentration, which will be derived from the GEO measurements. This helps in the quantitative interpretation of global images of the earth ring current and its spatial and temporal evolution (Williams, 1987).

The Geocoronal Imager on IMAGE (GEO) contains three photometers (Figure 20). An individual photometer is illustrated in Figure 21. It has a light baffle and MgF_2 lens and aperture plate. In a compartment separated by a MgF_2 window there is a ceramic channel electron multiplier. One of the three detectors looks outward in the spin plane and sweeps over the Earth once during each spin of the satellite. The other two tubes are tilted ±30° away from the spin plane and will mostly look past the Earth, except during perigee.

Figure 20. Geocorona Imager with its side removed to show a prototube. The sun sensor cluster is located in the middle of the front face of the instrument.

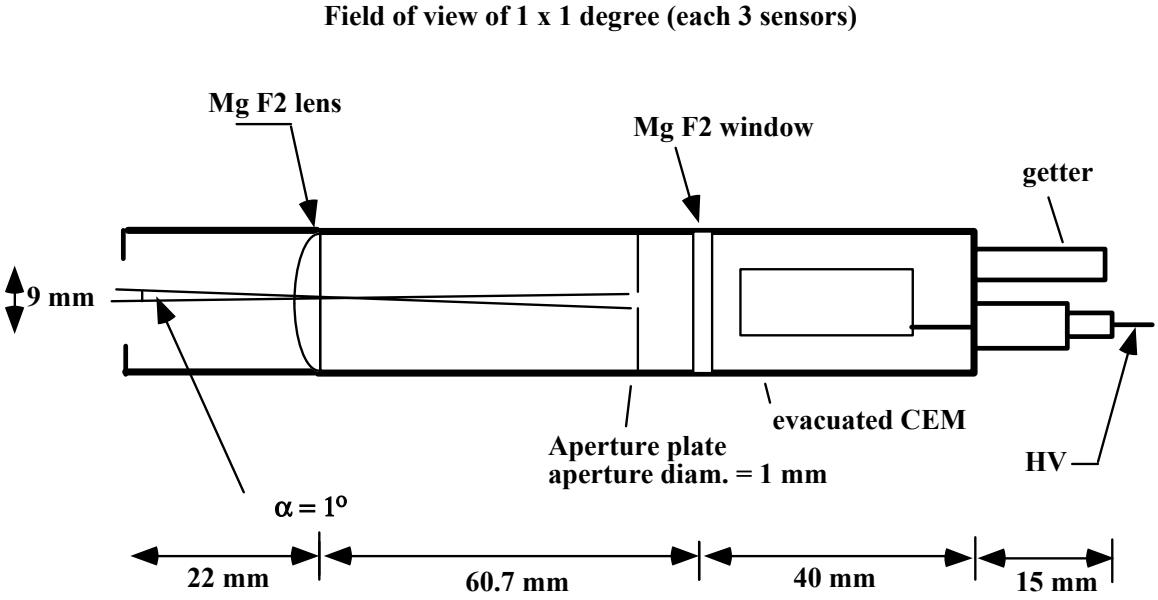

Figure 21. Single GEO detector tube with built in MgF_2 lens and aperture to limit the field of view to one degree.

A MgF_2 entrance lens of the photometers collects all the incoming photons and images them through a pinhole and a MgF_2 window into the channeltron. The combination of the MgF_2 transmission and the spectral sensitivity of the photocathode provides a bandpass between 115 and 150 nm (Figure 22).

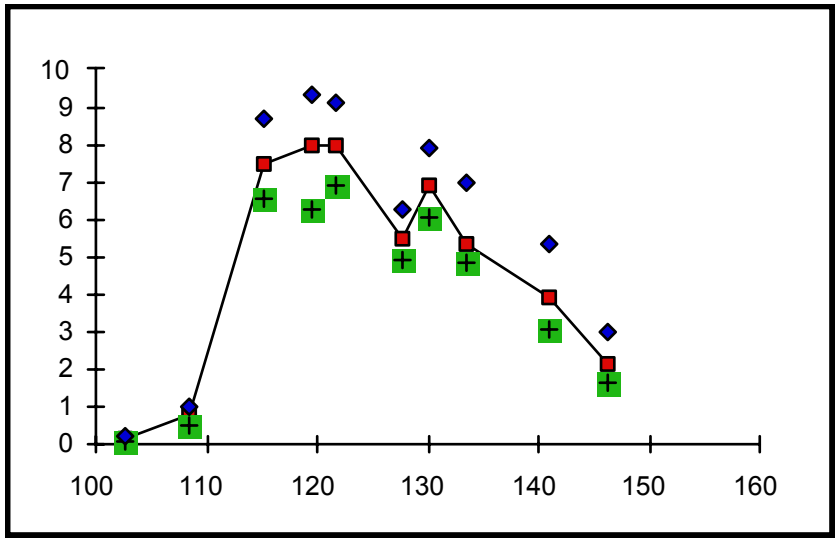

Figure 22. The effective quantum efficiency of a typical GEO detector in percent as a function of wavelength in nm. Mean, maximum and minimum of measurement errors are indicated.

The optical system of the tubes provides a spatial resolution of 1° (Figure 23). The integration time during flight will be 1/3 s and during this time the instrument platform will have rotated by 1°. The quantum efficiencies for Lyman-α radiation for the three tubes are between 4.2 and 7.9%. Therefore, we can expect count rates of more than 12 counts per second for 100 Rayleigh of source radiation.

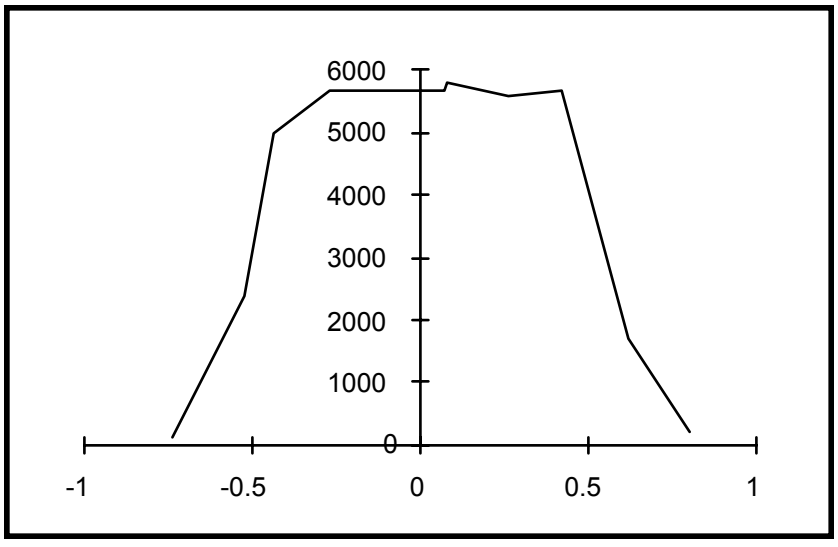

Figure 23. GEO angular response in raw counts as a function of the angle of the collimated beam entering the detector.

Depending on the geocentric distance of the satellite, column brightness of more than 10 kR can be expected (Rairden *et al.*, 1986). Even at apogee there is a background Lyman-α radiation of several Rayleigh from interplanetary and extragalactic neutral hydrogen (Ajello, 1990; Pryor et al., 1998).

The intensity of geocoronal Lyman-α line depends on the line center solar flux, which will not be measured by the IMAGE mission. However, since the emission is optically thick enough for multiple scattering to be important, the Lyman-α brightness measured by GEO as a function of spin angle (e.g., a zenith-to-nadir brightness profile) provides an independent measurement of the H density profile. In other words, getting a good fit to the shape of the Lyman-α signal as a function of look zenith angle provides the H profile. This would work at a single altitude, but GEO can do even better since it will get zenith angle scans at a wide range of altitudes. For a reference of this method, see, for example Anderson and Hord (1977), or Bush *et al.* (1995). Since this method removes the dependence on the solar Lyman-α flux (and for that matter, absolute instrumental sensitivity, since the shape is a relative measurement), solar variability will not affect the results. Currently the accuracy to which we will be able to determine the H density is not known yet. However in our modeling we will be using the state-of-the-art geocoronal Lyman-α code of Bishop (1999), and we expect the accuracy will be better than 20%. Our approach will be to fit the observed profiles to those predicted by the model and thereby obtain a parameterized model of the hydrogen distribution. The GEO resource requirements are summarized in Table 6.

Table 6
GEO sensor head resource requirements

Mass (kg)	Dimensions L x W x H (mm)	Standby power (W)	Acquire Power (W)
0.9	250 x 70 x 145	0.40	0.40

There are also 4 sun sensors incorporated into the GEO which have to assure the safe reduction of all instrument high voltages as soon as the sun enters the ±40° field of view of the sun sensor diodes. A direct illumination of the FUV detectors by full sunlight would damage the instruments, especially the photocathodes. There are two diodes sensitive to the visible part of the solar spectrum, and two sensitive to the UV part between 220 and 320 nm. While the Earth albedo in that part of the spectrum is quite low, the UV sensitive diodes will only trigger a high voltage reduction if the sun enters the field of view, but not the Earth. Depending on the cloud cover and topology of the Earth the visible diodes may create a quite large output signal if they observe the sunlit part of the Earth.

References

Ajello, J.M., Solar minimum Lyman-α sky background observations from Pioneer Venus orbiter ultraviolet spectrometer: Solar wind latitude variation, *J. Geophys. Res*., **95**, 14855-14861, 1990.

Anderson, D. E. and C. W. Hord, Multidimensional radiative transfer – Applications to planetary coronae, *Planet. Space Sci.*, **25**, 563-571, 1977.

Anger, C.D., J. S. Murphree, A. Vallance-Jones, R. A. King, A. L. Broadfoot, L. L. Cogger, F. Creutzberg, R. L. Gattinger, G. Gustafsson, F. R. Harris, J. W. Haslett, E. J. Llewellyn, J. C. McConnell, D. J. McEwen, E. H. Richardson, G. Rostoker, B. R. Sandel, G. G. Shepherd, D. Venkatesan, D. D. Wallis and G. Witt, Scientific results from the Viking ultraviolet imager: An introduction, *Geophys. Res. Lett.*, **14**, 383-386, 1987.

Basu, B., J. R. Jasperse, D. J. Strickland and R. E. Daniell, Transport-theoretic model for the electron-proton-hydrogen atom aurora, *J. Geophys. Res*., **98**, 21,517-21,532, 1993.

Bishop, J., Transport of resonant atomic hydrogen emissions in the thermosphere and geocorona: model description and applications, *J. Quantitative Spectroscopy and Radiative Transfer*, **61**, 473-491, 1999.

Bush, B. and S. Chakrabarti, Analysis of Lyman-α and He I 584-A airglow measurements using a spherical radiative transfer model, *J. Geophys. Res.*, **100**, 19,609-19,625, 1995.

Chamberlain, J. W., Planetary coronae and atmospheric evaportaion, *Planet Space Sci*., **11**, 901-960, 1963.

Eather R. H., Auroral proton precipitation and hydrogen emissions, *Rev. Geophys. and Space Phys*., **5**, 207-285, 1967.

Edgar, B. C.,W. T. Miles and A. E. S. Green, Energy deposition of protons in molecular nitrogen and application to proton auroral phenomena, *J. Geophys. Res.*, **78**, 6595-6606, 1973.

Frank, L. A. and J. D. Craven, Imaging results from Dynamics Explorer 1, *Reviews of Geophysics*, **26**, 249-283, 1988.

Galand, M. and A. D. Richmond, Magnetic mirroring in an incident proton beam, *J. Geophys. Res.*, **104**, 4447-4455, 1999.

Ishimoto, M., C. I. Meng, G. R. Romick and R. E. Huffman, Anomalous UV Auroral Spectra during a large magnetic disturbance, *J. Geophys. Res.*, **94**, 6955-6960, 1989.

Jasperse, J. R. and B. Basu, Transport theoretical solutions for auroral proton and H atom fluxes and related quantities, *J. Geophys. Res.*, **87**, 811-822, 1982.

Jelinsky, S. R., O. H. W. Siegmund and J. A. Mir, Progress in soft X-ray and UV photocathodes, *Proc. SPIE*, **2808**, 617-625, 1996.

Lampton, M. O. Siegmund and R. Raffanti, Delay line anodes for microchannel plate spectrometers, *Rev. Sci. Instrum*., **58**, 2298-2305, 1987.

Lampton, M., A timing discriminator for space flight applications, *Rev. Sci. Instrum.,* **69**, 3062-3065, 1998.

Lemaitre, M.-P., J. Laurent, J. Besson, A. Girard, C. Lippens, C. Muller, J. Vercheval and M. Ackerman, Sample performance of the grille spectrometer, *Science*, **225**, 171-172, 1984.

Loewen, E. G. and E. Popov, Diffraction gratings and applications, Marcel Dekker, Inc., New York, 1997, p.175ff.

Marov, M. Y., V. I. Shematovich, D.V. Bisikalo and J.C. Gerard, Nonequilibrium processes in the planetary and cometary atmospheres: Theory and applications, *Kluwer*, 1997.

Meier, R. R., Ultraviolet spectroscopy and remote sensing of the upper atmosphere, *Space Science Reviews*, **58**, 1-185, 1991.

Pryor, W. R., M. Witte and J.M. Ajello, Interplanetary Lyman-α remote sensing with the Ulysses Interstellar Neutral Gas Experiment, *J. Geophysics Res*., **103**, 26813-26831, 1998.

Rairden, R. L., L. A. Frank and J. D. Craven, Geocoronal imaging with Dynamics Explorer, *J. Geophys. Res.*, **91**, 13613-13630, 1986

Siegmund, O. H. W. and J. Stock, Performance of low resistance microchannel plate stacks, *Proc. SPIE*, **1549**, 81-89, 1991.

Siegmund, O. H.W., *et al.*, Delay line detectors for the UVCS and SUMER instruments on the SOHO satellite, *Proc. SPIE*, **2280**, 89-100, 1994.

Stock, J. M., O. H. W. Siegmund, J. S. Hull, K. E. Kromer, S. R. Jelinsky, H. D. Heetderks, M. L. Lampton, and S. B. Mende, Cross delay line microchannel plate detectors for the Spectrographic Imager on the IMAGE satellite, *Proc. SPIE,* **3445**, 407-414, 1998.

Strickland, D. J. and D. E. Anderson, Jr., Radiation transport effects on the OI 1356-AA limb intensity profile in the dayglow, *J. Geophys. Res.*, **88**, 9260-9264, 1983.

Strickland, D. J., J. R. Jasperse and J.A. Whalen, Dependence of auroral FUV emissions on the incident electron spectrum and neutral atmosphere, *J. Geophys. Res*., **88**, 8051-8062, 1983.

Strickland, D. J., R. E. Danielle, Jr., J. R. Jasperse and B. Basu, Transport-theoretic model for the electron-proton-hydrogen atom aurora: 2. Model results, *J. Geophys. Res*., **98**, 21,533-21,548, 1993.

Torr, M. R., D. G. Torr, M. Zukic, R. B. Johnson, J. Ajello, P. Banks, K. Clark, K. Cole, C. Keffer, G. Parks, B. Tsurantani and J. Spann, A far ultraviolet imager for the International Solar-Terrestrial Physics mission, *Space Science Reviews*, **71**, 329, 1995.

Williams, D. J., Ring current and radiation belts, *Rev. Geophys.*, **25**, 570-578, 1987.